RSC Advances

PAPER

View Article Online
View Journal | View Issue

Cite this: *RSC Adv.*, 2025, **15**, 36607

First-principles study on enhancing the photocatalytic hydrogen evolution performance in $Cs_3Bi_2I_9/MoS_2$ heterostructure with interfacial defect engineering

Kyong-Mi Kim,[a] Yun-Sim Kim,[a] Dok-Ho Hyon,[b] Chol-Hyok Ri[ac] and Chol-Jun Yu *[a]

Hydrogen has been attracting continuously growing interest as a highly efficient and clean energy source for replacing fossil fuels in the future, and thus developing highly efficient photocatalytic materials for hydrogen evolution is much desirable. In this work, we study the structural, electronic and optical properties of heterostructures composed of the bismuth-based vacancy-ordered iodide double perovskite $Cs_3Bi_2I_9$ and a two-dimensional dichalcogenide 2H-MoS_2 monolayer without and with a vacancy defect using first-principles calculations. Our calculations demonstrate that the $Cs_3Bi_2I_9/MoS_2$ heterostructures are energetically stable and induce an interfacial dipole moment, which is beneficial for the prevention of charge carrier recombination. Due to the proper band-edge alignment and the smallest Gibbs free energy difference for hydrogen adsorption, the defective interface with a Cs-vacancy (V_{Cs}) is found to be the most promising for photocatalytic hydrogen evolution. Moreover, we find that the interfacial V_{Cs} defect can be formed favourably under the I-rich/Cs-poor condition, where V_I and V_S formations are suppressed. This work provides a way to develop high-performance photocatalysts based on heterostructures composed of the Bi-based halide perovskites and transition metal dichalcogenides for hydrogen evolution from solar-driven water splitting.

Received 22nd July 2025
Accepted 5th September 2025

DOI: 10.1039/d5ra05294g

rsc.li/rsc-advances

1 Introduction

Superseding natural resources with clean sustainable energy sources has become an extremely urgent issue to meet the increasing demand for energy and achieve net-zero carbon emissions in light of the rapid exhaustion of fossil fuels and acute environmental problems. In this context, hydrogen has been attracting continuously growing interest as a highly efficient and clean energy source for the future.[1] Among various methods for producing hydrogen, solar-driven photocatalytic hydrogen evolution is the most attractive approach in terms of energy balance and clean production due to solar energy utilization.[2–4] Photocatalysts for hydrogen evolution reactions (HERs) reported so far include carbon nitrides,[5–7] metal oxides,[8,9] metal sulfides,[10–12] organic materials,[13,14] and heterojunctions.[15,16] When using those photocatalysts, however, the solar-to-hydrogen (STH) conversion efficiencies are still far below the target threshold of ~10% required for commercialization.[17] To increase the STH efficiency towards 10%, many strategies have been developed, including the search for new materials, heteroatom doping, interface engineering and phase engineering.[18]

Since their first use as light absorbers in solar cells in 2009,[19] halide perovskites (HPs) have been attracting significant attention in the field of photovoltaics, with high power conversion efficiencies exceeding 27% being reported.[20–23] This is due to the superior optoelectronic properties of HPs, including strong light absorption,[24] tunable bandgap,[25] long carrier lifetime,[26] long carrier diffusion lengths[27,28] and high carrier mobility.[29] The best-known photocatalysts for HERs are lead-containing HPs,[30] which are usually used in the form of heterojunctions with other photocatalysts to prevent the serious recombination of photogenerated charge carriers. As reported by Zhao *et al.*,[31] the organic–inorganic hybrid HP $MAPbI_3$ (MA = CH_3NH_3, methylammonium), when integrated with a MoS_2 monolayer, demonstrated a STH efficiency of 1.09% and prominent hydrogen generation activity (HGA) of 13.6 mmol g^{-1} h^{-1}. By integrating a polyfluorene co-catalyst onto the surface of $MAPbI_3$, Pal *et al.*[32] reported a HGA of up to 6.2 mmol g^{-1} h^{-1} in HI solution, almost 200-fold higher than that of pristine $MAPbI_3$. In spite of such outstanding photovoltaic and photocatalytic properties, the organic–inorganic hybrid HPs have suffered from poor stability due to the existence of the organic moiety.[33] Therefore, the organic species (*e.g.*, MA) were replaced

[a]*Computational Materials Design, Faculty of Materials Science, Kim Il Sung University, Taesong District, Pyongyang, Democratic People's Republic of Korea. E-mail: cj.yu@ryongnamsan.edu.kp*

[b]*Institute of Nano Engineering, State Academy of Science, Rakrang District, Pyongyang, Democratic People's Republic of Korea*

[c]*Faculty of Physics, O Jung Hup Chongjin University of Education, Chongjin, North Hamgyong Province, Democratic People's Republic of Korea*

with inorganic ones; for instance, $CsPb(Br_{1-x}I_x)_3$ with a noble metal co-catalyst of Pt demonstrated a HGA value of 1.12 mmol g^{-1} h^{-1} in the HI/HBr mixed solution.[34]

In the Pb-based HPs, toxicity of lead is another problem, causing environmental and health care concerns. To address these problems, several metals, such as Sn, Ge and Bi, can be used instead of Pb in the all-inorganic HPs.[35–37] Typically, Bi-based HPs have been utilized in photocatalytic and photovoltaic applications due to their optoelectronic properties being comparable with Pb-based ones, including good intrinsic stability and eco-friendliness.[38,39] For instance, $Cs_3Bi_2Br_9$ nanocrystals coupled with graphitic carbon nitride (g-C_3N_4) nanosheets were found to exhibit a good HGA of 4.6 mmol g^{-1} h^{-1}.[40] Moreover, Pancielejko *et al.*[41] have demonstrated a 24-fold improvement in HGA by combining Bi-based HPs of $Cs_3Bi_2X_9$ (X = I, Br, Cl) with different types of TiO_2. Tang *et al.*[42] also reported an improved photocatalytic performance for a $Cs_3Bi_2I_9/Ti_3C_2$ composite due to the promoted charge transfer and separation. A stable composite of $Cs_3Bi_2I_9$ and MoS_2 quantum dots has also been reported to show great enhancement in photocatalytic performance,[43] achieving a HGA of 6.09 mmol g^{-1} h^{-1}, which notably surpasses that of pristine $Cs_3Bi_2I_9$ and Pt/$Cs_3Bi_2I_9$ composite by 8.8 and 2.5 times, respectively. Such an impressive improvement, leading to a new record for Bi-based HP photocatalysts under visible light, was attributed to the type-II heterojunction between $Cs_3Bi_2I_9$ and MoS_2.

The experimental findings mentioned above highlight the importance of interface engineering in enhancing the photocatalytic performance of Bi-based HP photocatalysts. To fully understand the underlying mechanism of such an enhancement through interface formation, a first-principles study based on density functional theory (DFT) is necessary.[16] Since the photocatalytic performance encompasses both the intrinsic properties and the efficiency of a photocatalyst, one should clarify the electronic and optical properties such as band structure, band-edge alignment against the water redox potential, photoabsorption coefficients and the Gibbs free-energy difference upon hydrogen adsorption on the catalysis surface to estimate the photocatalytic performance, which further determines the STH conversion efficiency or HGA. To the best of our knowledge, however, no theoretical studies on the $Cs_3Bi_2I_9/MoS_2$ heterostructure have been reported to date, meaning that the effects of interface and defect engineering on its photocatalytic performance remain unclear. In this work, we perform first-principles calculations of the $Cs_3Bi_2I_9/MoS_2$ heterostructure to gain atomistic insights into the interfacial and defect effects on the electronic and optical properties. In particular, we consider typical vacancy defects at the interface, evaluating their formation energies, various interfacial properties and HER performance.

2 Methods

2.1 Computational methods

In the early steps, the DFT calculations were performed by using the pseudopotential plane-wave method as implemented in the Quantum ESPRESSO (QE, version 7.2) package.[44] For describing the ion–electron interactions, we used the ultrasoft pseudopotentials provided in the GBRV library,[45] which were generated with scalar relativistic calculations by using the valence electron configurations of Cs-$5s^25p^66s^1$, Bi-$6s^26p^35d^{10}$, I-$5s^25p^5$, Mo-$4s^24p^65s^24d^4$ and S-$3s^23p^4$. The Perdew–Burke–Ernzerhof (PBE) formalism[46] within the generalized gradient approximation (GGA) was used for the exchange–correlation interaction. Since the interface systems under study include layered materials of MoS_2 and $Cs_3Bi_2I_9$, the van der Waals (vdW) interactions between the layers were taken into account by using the vdW-DF-ob86 functional.[47] As the major computational parameters, the kinetic cutoff energies were set to 40 and 400 Ry for wave functions and electron density, respectively, and the special *k*-point meshes for the Brillouin zone sampling were set to $(4 \times 4 \times 2)$. All the atomic positions were relaxed until the residual force on the atom converged to 5×10^{-4} Ry per Bohr, while the crystalline lattice was optimized until the stress was less than 0.05 kbar.

For the supercell calculations to consider the interfacial defects, the pseudo-atomic orbital (PAO) basis sets method as implemented in the SIESTA (version 4.1) package[48] was used. We selected the double-ζ plus polarization (DZP) scheme for the PAO basis sets, which were generated using an energy shift of 300 meV for the orbital-confining cutoff radii and a split norm of 0.30 for the split-valence. The plane-wave cutoff energy was set to 100 Ry and the special *k*-points mesh was set to $(4 \times 4 \times 1)$ for atomic relaxations and $(6 \times 6 \times 1)$ for energetic and optical calculations. The atomic relaxations were performed until the atomic forces converged to 0.02 eV $Å^{-1}$. We note that such calculations using the combination of QE and SIESTA packages were found to give reasonable results for different interface systems, with an affordable computational cost.[16,49–51]

The formation energy of a vacancy defect i with charge q was calculated as follows:[52,53]

$$E_f(i,q) = E_{tot}(i,q) - E_{perf} + \mu_i + q(E_F + E_{VBM}), \quad (1)$$

where E_{perf} and $E_{tot}(i,q)$ are the DFT total energies of the perfect supercell and the defective supercell containing one vacancy defect i with a charge state q, E_F is the Fermi energy referenced to the energy level of the valence band maximum (VBM) E_{VBM}, and μ_i is the chemical potential of the i-th species removed from the supercell. The chemical potential μ_i can be written as $\mu_i = E_i + \Delta\mu_i$, where E_i is the total energy per atom of the corresponding simple substance. Under the thermodynamic equilibrium condition, the existence of bulk $Cs_3Bi_2I_9$ and MoS_2 puts constraints on the chemical potentials as follows:[51,54,55]

$$\Delta E_{Cs_3Bi_2I_9} = 3\Delta\mu_{Cs} + 2\Delta\mu_{Bi} + 9\Delta\mu_I, \quad (2)$$

$$\Delta E_{MoS_2} = \Delta\mu_{Mo} + 2\Delta\mu_S, \quad (3)$$

where $\Delta E_{Cs_3Bi_2I_9} = (E^{bulk}_{Cs_3Bi_2I_9} - 3E^{bulk}_{Cs} - 2E^{bulk}_{Bi} - 9E^{bulk}_{I})$ and $\Delta E_{MoS_2} = (E^{bulk}_{MoS_2} - E^{bulk}_{Mo} - 2E^{bulk}_{S})$ are the formation energies of the $Cs_3Bi_2I_9$ and MoS_2 compounds, respectively. To prevent the formation of elemental bulk i, the condition $\Delta\mu_i < 0$ should be satisfied. To ensure the formation of $Cs_3Bi_2I_9$ from the binary compounds CsI and BiI_3, the following constraints must be met:

$$\Delta\mu_{Cs} + \Delta\mu_{I} < \Delta E_{CsI} \quad (4)$$

$$\Delta\mu_{Bi} + 3\Delta\mu_{I} < \Delta E_{BiI_3} \quad (5)$$

For other binary compounds, such as CsI_3, CsI_4, Bi_9I_2, Cs_3Bi, CsBi and $CsBi_2$, similar constraints are satisfied. Moreover, chemical dissociation of $Cs_3Bi_2I_9$ into the binary constituents (CsI and BiI_3) should be prohibited and thus the following condition should be satisfied:

$$\Delta E_{Cs_3Bi_2I_9} - 3\Delta E_{CsI} < 2\Delta\mu_{Bi} + 6\Delta\mu_{I} < 2\Delta E_{BiI_3} \quad (6)$$

The hydrogen adsorption energy ΔE_H is determined as[56]

$$\Delta E_H = E_{sub+H} - E_{sub} - \frac{1}{2}E_{H_2}, \quad (7)$$

where E_{sub+H} and E_{sub} are the total energies of the substrate systems with and without an adsorbed H atom on the surface, respectively, and E_{H_2} is the total energy of an isolated H_2 molecule placed in a supercell of the same size as the substrate system, which is large enough to neglect the artificial interactions between the molecule and its periodic images. Then, the Gibbs free energy of hydrogen adsorption ΔG_{H^*} can be evaluated as follows:

$$\Delta G_{H^*} = \Delta E_H + \Delta E_{ZPE} - T\Delta S_H, \quad (8)$$

where ΔE_{ZPE} is the difference between the zero-point energy (ZPE) of H_2 in the adsorbed state and that in the gas-phase state, and ΔS_H is the difference in entropy of H_2 between the gas phase and adsorbed state. Here, ΔS_H can be written as $\Delta S_H = -\frac{1}{2}S_{H_2^\circ}$, where $S_{H_2^\circ}$ is the entropy of H_2 under standard conditions. We utilized 0.24 eV for $\Delta E_{ZPE} - T\Delta S_H$, as reported in the previous work for hydrogen adsorption.[56]

The imaginary and real parts of the frequency-dependent complex dielectric function, $\varepsilon(\omega) = \varepsilon_1(\omega) + i\varepsilon_2(\omega)$, were calculated using the density functional perturbation theory (DFPT) as implemented in the SIESTA package.[48,57] Then, the optical absorption coefficients $\alpha(\omega)$ were obtained as follows:[58–60]

$$\alpha(\omega) = \frac{2\omega}{c}\sqrt{\frac{\sqrt{\varepsilon_1{}^2(\omega) + \varepsilon_2{}^2(\omega)} - \varepsilon_1(\omega)}{2}}, \quad (9)$$

where c is the speed of light.

2.2 Interface modelling

As a layered vacancy-ordered double perovskite, $Cs_3Bi_2I_9$ is crystallized in a hexagonal lattice with a space group of $P6_3/mmc$ under ambient conditions,[61] as shown in Fig. 1(a). The structure of $Cs_3Bi_2I_9$ is characterized by two neighboring $[Bi_2I_9]^{3-}$ octahedra, which are face-shared along the c-axis to form a $[Bi_2I_9]^{3-}$ bioctahedral cluster, and the $[Bi_2I_9]^{3-}$ clusters are separated by hexagonal channels filled with Cs^+ cations, leading to the formation of a zero-dimensional molecular salt crystal structure. Within the $[Bi_2I_9]^{3-}$ bioctahedral cluster, there exist three long bridging Bi–I bonds, which involve I atoms on the shared face, and six terminal short Bi–I bonds oriented away from the shared face. For MoS_2 bulk, we selected the 2H phase among its polymorphs, which is also in a hexagonal lattice with the space group of $P6_3/mmc$. With the optimized bulk structures, we built the interface slab models of $Cs_3Bi_2I_9$ (001) surface and MoS_2 (001) monolayer (ML). According to the experimental report for the structural characteristics,[62] the $Cs_3Bi_2I_9$ (001) surface was suggested to have CsI_3 termination. To minimize the lattice mismatch between the $Cs_3Bi_2I_9$ (001) and MoS_2 (001) surfaces, we applied the coincidence lattice method.[63] As a result, we obtained the surface supercells along the lines of [310] and [230] for 2H-MoS_2 (Fig. 1(c)) and [100] and [110] for $Cs_3Bi_2I_9$ (Fig. 1(d)), with a significantly small lattice mismatch of 0.1% evaluated as follows:[64]

$$\eta = \frac{2|a_1 - a_2|}{a_1 + a_2}, \quad (10)$$

where a_1 and a_2 are the lattice constants of the $Cs_3Bi_2I_9$ and 2H-MoS_2 lattices. The resultant supercells correspond to (1×1) and (7×7) for $Cs_3Bi_2I_9$ (001) and 2H-MoS_2 (001) surfaces, respectively. The slab models of the interface contained ten atomic layers of $Cs_3Bi_2I_9$ and an S–Mo–S layer of MoS_2 (49 atoms) with a vacuum layer of 15 Å thickness, as shown in Fig. 1(e). We confirm that the 10 atomic layers for the $Cs_3Bi_2I_9$ is thick enough to guarantee convergence of the surface energy and the 15 Å vacuum thickness is sufficiently large to inhibit the artificial interactions between the top and bottom atoms of the neighbouring slabs. While fixing the lattice constants of the slab supercell and the atomic positions of the 6 atomic layers in the $Cs_3Bi_2I_9$ side, all other atomic positions were relaxed using the QE code. Here, we considered two different possible sliding structures between $Cs_3Bi_2I_9$ and MoS_2, denoted as Conf1 and Conf2 (Fig. S2, SI), and performed atomic relaxations for these sliding configurations. From the calculation, the Conf1 sliding structure, where one of the S atoms in the MoS_2 layer is placed on top of the Cs atom of the $Cs_3Bi_2I_9$, was found to have a lower total energy with a shorter interlayer binding distance than the Conf2 structure. Therefore, we only considered the Conf1 sliding structure for further calculations of the electronic and photocatalytic properties.[65]

In order to consider the vacancy defects, we built $2 \times 2 \times 1$ supercells (196 atoms) with a very thick vacuum layer (70 Å) using the relaxed interface slabs with the QE code. The atomic relaxations were also performed using the SIESTA code, while fixing the lattice constants and the 6 atomic layers of the $Cs_3Bi_2I_9$ side. We confirm that the supercell sizes are large enough for defect calculations as used in the previous works.[16,66] Then, each of the three types of interfacial vacancy defect, such as caesium (V_{Cs}), iodine (V_I) and sulfur (V_S), was created at different positions around the interface, and the lowest energy configuration for each defect was identified by performing the atomic relaxation (see Fig. S3 and Table S1, SI). We considered different charge states for each vacancy defect in this work.

The formation energy of the interface is defined as follows:[67]

$$E_f = \frac{1}{A}\left(E^{int}_{Cs_3Bi_2I_9/MoS_2} - E^{surf}_{Cs_3Bi_2I_9} - E^{surf}_{MoS_2}\right), \quad (11)$$

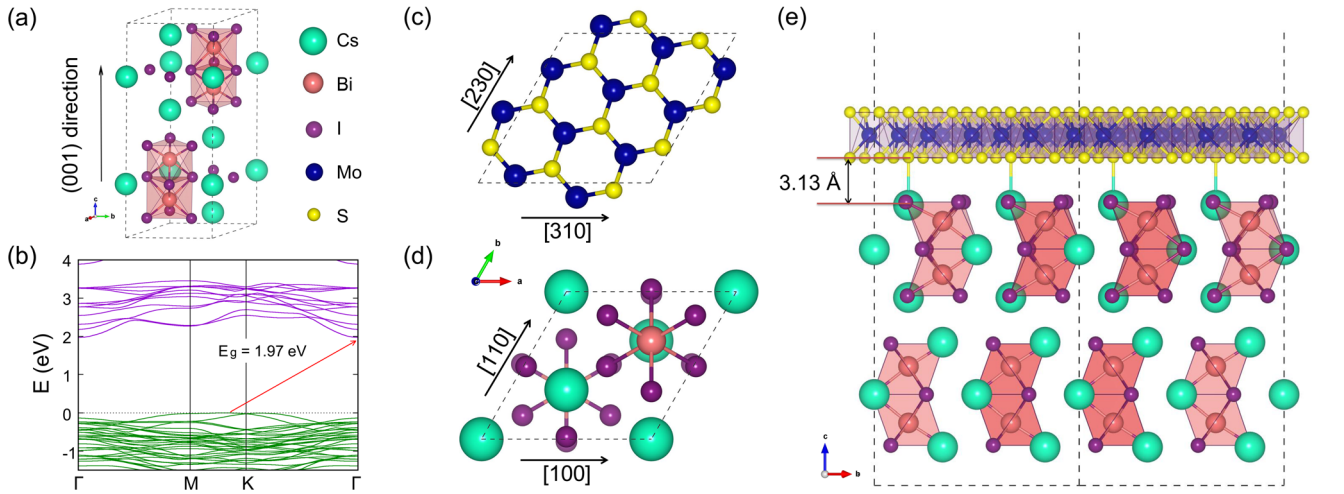

Fig. 1 (a) Polyhedral view of the unit cell for the $Cs_3Bi_2I_9$ crystal optimized with QE. (b) Electronic band structure of the bulk $Cs_3Bi_2I_9$ calculated in this study. Top view of the lattice-matched structure of (c) the MoS_2 (001) surface (7 × 7) supercell and (d) the $Cs_3Bi_2I_9$ (001) surface unit cell. (e) Side view of the $Cs_3Bi_2I_9/MoS_2$ ML interface supercell model relaxed with SIESTA.

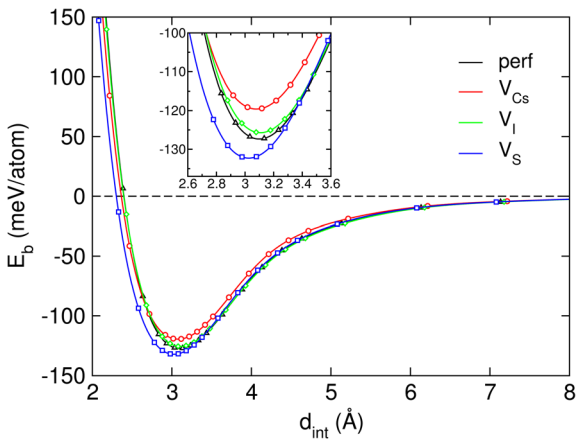

Fig. 2 The interlayer binding energy per atom E_b for the $Cs_3Bi_2I_9/MoS_2$ heterojunction as a function of interlayer binding distance d_{int}. The inset represents the magnified view around the equilibrium distance d_{eq}.

Table 1 The interface formation energy E_f, interlayer binding energy E_b and interlayer equilibrium distances d_{int} in the $Cs_3Bi_2I_9/MoS_2$ heterostructures without and with vacancy defects

System	E_f (J m^{-2})	E_b (meV per atom)	d_{int} (Å)
Perfect	−0.70	−127.82	3.13
V_{Cs}		−117.95	3.22
V_I		−125.81	3.18
V_S		−132.54	3.08

where $E^{int}_{Cs_3Bi_2I_9/MoS_2}$, $E^{surf}_{Cs_3Bi_2I_9}$ and $E^{surf}_{MoS_2}$ are the DFT total energies of the $Cs_3Bi_2I_9/MoS_2$ interface, the $Cs_3Bi_2I_9$ (001) surface and the MoS_2 (001) surface, respectively, and A is the interface area. The total energies for the surfaces were calculated by using the fully relaxed isolated surface systems with the same cell size with the interface. The interlayer binding energy is defined as follows:

$$E_b = \frac{1}{N}\left(E^{int}(d_{eq}) - E^{int}(d_\infty)\right), \quad (12)$$

where $E^{int}(d_{eq})$ and $E^{int}(d_\infty)$ are the total energies of the interface systems with the equilibrium interlayer distance and the infinity distance, respectively, and N is the number of atoms in the MoS_2 layer. The spatial charge density difference was evaluated as follows:

$$\Delta\rho = \rho_{int} - \rho_{Cs_3Bi_2I_9} - \rho_{MoS_2}, \quad (13)$$

where ρ_{int}, $\rho_{Cs_3Bi_2I_9}$ and ρ_{MoS_2} are the charge densities of the interface, isolated $Cs_3Bi_2I_9$ and MoS_2 surface sides, respectively. Then, the planar-averaged charge density difference integrated on the $x-y$ plane was calculated as follows:

$$\Delta\bar{\rho}(z) = \frac{1}{A}\int_A \Delta\rho(x,y,z)\mathrm{d}x\mathrm{d}y, \quad (14)$$

where A is the area of the $x-y$ plane.[16,51]

3 Results and discussion

3.1 Structural stability of the interface

Firstly, we scrutinized the geometrical and electronic properties of bulk $Cs_3Bi_2I_9$ and 2H-MoS_2. By performing the structural optimizations of the unit cells, we determined their lattice constants to be $a = b = 8.371$ Å, $c = 21.132$ Å for $Cs_3Bi_2I_9$ and $a = b = 3.167$ Å, $c = 12.374$ Å for 2H-MoS_2, which agree well with the previous experimental results.[61,68,69] Using the QE code with the PBE functional, we then calculated their electronic band structures. Fig. 1(b) shows the calculated band structure of $Cs_3Bi_2I_9$, demonstrating an indirect bandgap of 1.97 eV in good agreement with the previous results.[61,70] Meanwhile, the band structure of the 2H-MoS_2 monolayer shows a direct bandgap of 1.84 eV, also in good agreement with the previous DFT

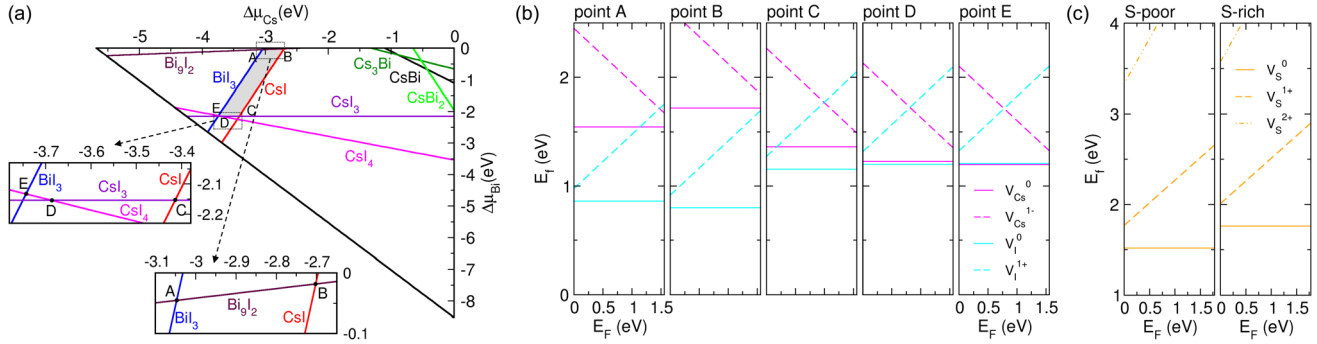

Fig. 3 (a) Chemical potential ranges of Cs and Bi for the stable $Cs_3Bi_2I_9$ compound, marked as grey-colored pentagon ABCDE. Outside the pentagon, the other binary compounds such as CsI, BiI_3, CsI_3, CsI_4, Bi_9I_2, CsBi, Cs_3Bi and $CsBi_2$ will form instead of the $Cs_3Bi_2I_9$ perovskite. Insets depict the magnified views around the vertexes of the pentagon. (b) Calculated formation energies of V_{Cs} and V_I defects at the$Cs_3Bi_2I_9$ part of the interface as a function of the Fermi energy (E_F) at points A, B, C, D and E. (c) The formation energy of vacancy defect V_S at the MoS_2 part of the interface under S-poor and S-rich conditions.

calculations[69] (see Fig. S1, SI). Such good agreements indicate that the computational settings employed in this work are reasonably acceptable. We note that the GGA-PBE functional was found to give bandgap values that agreed well with the experimental ones for lead halide perovskites, due to the fortuitous error compensation between the underestimation of PBE and overestimation by ignoring the spin–orbit coupling effect.[71,72]

With these calculated lattice constants of the bulk materials, the cell dimensions of the $Cs_3Bi_2I_9/MoS_2$ interface were found to be 8.375 × 8.375 Å and those of the 2 × 2 supercells was 16.75 × 16.75 Å. To estimate the stability of the $Cs_3Bi_2I_9/MoS_2$ interface system, the formation energy E_f was calculated. The formation energy was found to be negative, indicating that the formation of the $Cs_3Bi_2I_9/MoS_2$ interface is exothermic and that binding between the constituent $Cs_3Bi_2I_9$ surface and MoS_2 monolayer is energetically favorable. In fact, the formation energy of the

Table 2 Transferred charge upon the formation of the $Cs_3Bi_2I_9/MoS_2$ heterostructures under study, which is divided into contributions from each of the subsystems ($\Delta q_{Cs_3Bi_2I_9}$, Δq_{MoS_2}), and the interfacial dipole moment $\Delta\mu$

System	Δq_{Cs_3Bi2I9} (|e|)	Δq_{MoS_2} (|e|)	$\Delta\mu$ (Debye)
Perfect	−0.306	0.308	4.23
V_{Cs}	−0.202	0.204	2.41
V_I	−0.318	0.321	4.79
V_S	−0.250	0.254	4.29

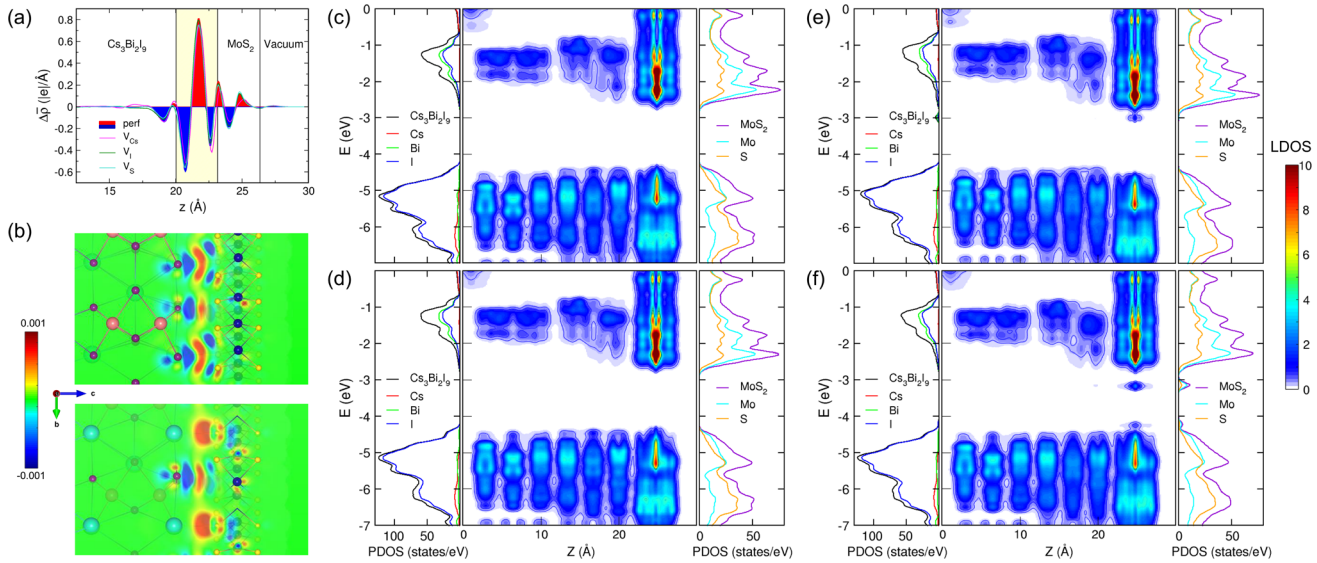

Fig. 4 (a) Planar-averaged charge density difference ($\Delta\bar{\rho}$) integrated over the x–y plane along the z-axis upon the formation of $Cs_3Bi_2I_9/MoS_2$ interfaces without and with the vacancy defects under study. (b) Isosurface plot of the spatial charge density difference upon the formation of the perfect interface projected on the (100) planes passing the I atoms (top panel) and Cs atoms (bottom panel) of the $Cs_3Bi_2I_9$ surface, ranging from 0.001 to 0.001 |e| $Å^{-3}$. Partial density of states (PDOS) and isosurface and isoline plots of local density of states (LDOS) for (c) the perfect interface, (d) V_{Cs}-, (e) V_I- and (f) V_S-containing interfaces.

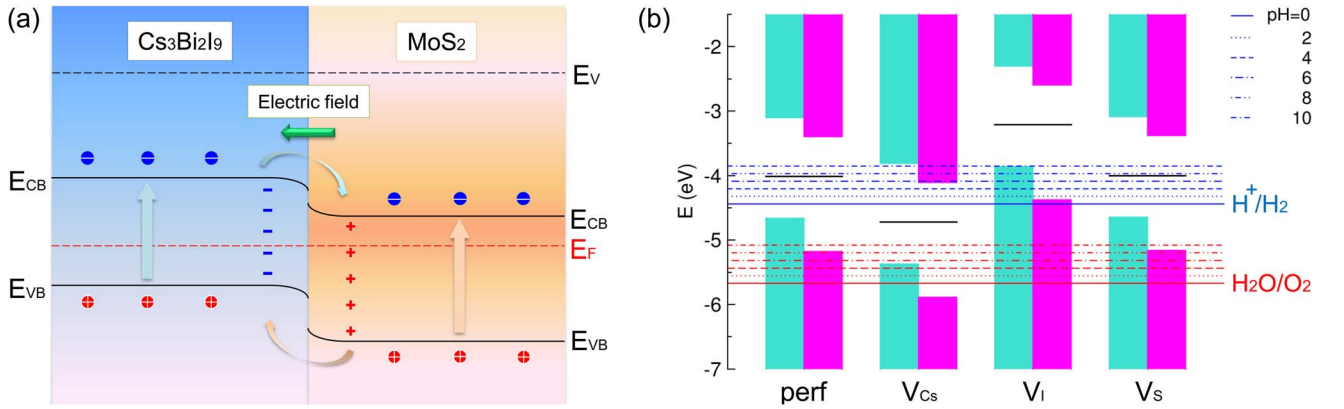

Fig. 5 (a) Schematic diagram of band alignment in the $Cs_3Bi_2I_9/MoS_2$ interface with a type-II heterojunction. Here, E_v and E_F are the vacuum and Fermi energy levels, and E_{VB} and E_{CB} are the VBM and CBM levels of the $Cs_3Bi_2I_9$ and MoS_2 sides. (b) Band-edge alignments of $Cs_3Bi_2I_9/MoS_2$ interface systems, referenced to the vacuum level. Turquoise and magenta bars indicate VBs and CBs of the $Cs_3Bi_2I_9$ and MoS_2 parts, respectively. The Fermi level is depicted as a horizontal black line for each interface system. Blue and red horizontal long lines represent the hydrogen reduction and water oxidation potentials, respectively, at different pH values.

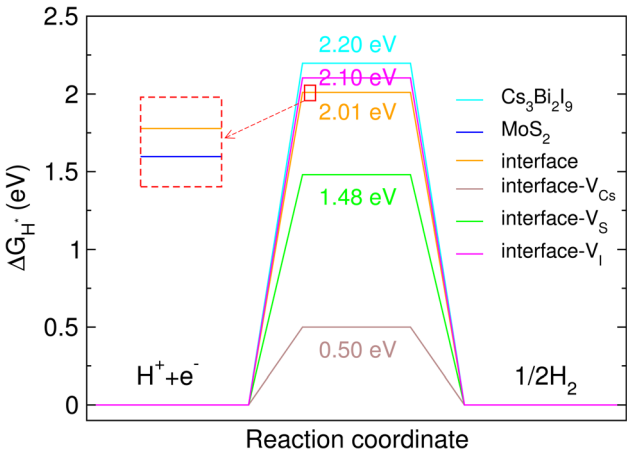

Fig. 6 Gibbs free energy difference for hydrogen adsorption (ΔG_{H^*}) on the $Cs_3Bi_2I_9/MoS_2$ interface systems without and with the vacancy defects such as V_{Cs}, V_I and V_S, together with those on the pristine $Cs_3Bi_2I_9$ surface and MoS_2 monolayer.

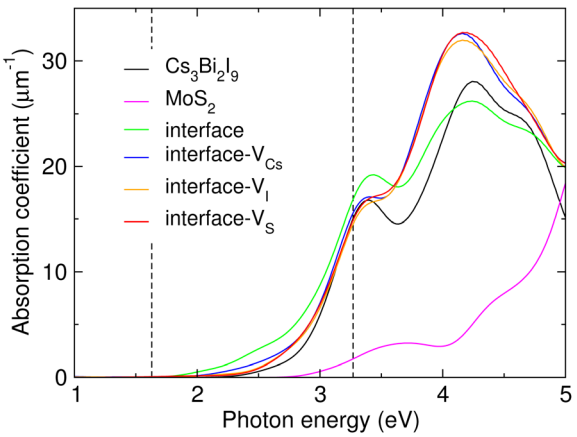

Fig. 7 Photoabsorption spectra of bulk $Cs_3Bi_2I_9$, the MoS_2 monolayer and the $Cs_3Bi_2I_9/MoS_2$ interface systems without and with a vacancy defect. The vertical dashed lines indicate the visible-light region.

perfect heterostructure without any defects was calculated to be -0.70 J m^{-2}, being lower than that of the $CsPbI_3/MoS_2$ interface obtained in our previous work[16] (-0.22 and -0.37 J m^{-2} for CsI and PbI_2 terminations, respectively). This indicates the stronger binding between the constituent layers in the $Cs_3Bi_2I_9/MoS_2$ heterostructure than in the $CsPbI_3/MoS_2$ heterostructure.

To further assess the binding strength between the constituent layers of the interface, the interlayer binding energy was also calculated. Fig. 2 shows the resultant E_b as a function of interlayer distance d_{int}. Table 1 lists the calculated values for the interface formation energy, interlayer binding energies and interlayer equilibrium distances for the $Cs_3Bi_2I_9/MoS_2$ heterostructures considered in this work. Irrelevant to the existence of vacancy defects, the binding energy E_b values for the interface systems were found to be negative, indicating the attractive binding in the $Cs_3Bi_2I_9/MoS_2$ interface systems. The binding energy for the perfect system was estimated to be -127.81 meV per atom, which is comparable to that of the $CsPbI_3/MoS_2$ interface.[16,73] Among the different defective systems, the V_S interface system was found to have the lowest binding energy of -132.54 meV per atom and accordingly the shortest interlayer distance of 3.08 Å. For the cases of V_I and V_{Cs}, the E_b values were found to slightly increase to -125.81 and -117.95 meV per atom, while the d_{int} values decrease to 3.18 and 3.22 Å, respectively.

3.2 Formation of interfacial vacancy defect

Defects play a decisive role in the photovoltaic and photocatalytic applications. To check the formation possibility of the interfacial vacancy defects under the synthesis conditions, we estimated their formation energies from the thermodynamic point of view. According to eqn (1), the defect formation energy varies with the chemical potentials of the elements, which reflect the synthesis conditions in the experiments. Therefore, we first determined the chemical potential ranges of all the

species included in the interface system for ensuring the stable existence of bulk $Cs_3Bi_2I_9$ and MoS_2 by using the thermodynamic constraints given by eqn (2)–(6) and the formation energy values of the available compounds (see Table S2 and Fig. S4, SI). Note that none of the ternary compounds are available in the Cs-Bi-I system, except for $Cs_3Bi_2I_9$.

Fig. 3(a) presents the chemical potential diagram obtained in this work concerning the chemical potentials of Cs ($\Delta\mu_{Cs}$) and Bi ($\Delta\mu_{Bi}$), which are referenced to those of the corresponding elemental bulks. The thermodynamically stable region for the $Cs_3Bi_2I_9$ compound is marked as the grey-colored region shown as the pentagon ABCDE (see Table S3 for the chemical potential values at the five vertexes of the pentagon, ESI). Among the vertex points of the pentagon, point B has the maximum value of $\Delta\mu_{Cs}$ and the minimum value of $\Delta\mu_I$ ($\Delta\mu_{Cs} = -2.70$ eV, $\Delta\mu_{Bi} = 0.02$ eV, $\Delta\mu_I = -0.99$ eV), while point E has the maximum value of $\Delta\mu_I$ and the minimum value of $\Delta\mu_{Cs}$ ($\Delta\mu_{Cs} = -3.74$ eV, $\Delta\mu_{Bi} = -2.13$ eV, $\Delta\mu_I = -0.17$ eV). Therefore, point B is said to represent the Cs-rich/I-poor condition, while point E represents the I-rich/Cs-poor condition. The possible chemical potential ranges for Mo and S species were also evaluated (see Table S3, SI). Note that outside of the pentagon region, the undesirable binary compounds such as CsI, BiI_3, CsI_3 and CsI_4 are more stable than $Cs_3Bi_2I_9$. For instance, BiI_3 will form in the left-hand side of the A–E line, while the CsI compound is stable in the right-hand side of the B–C line. It is worth noting that the stable region has a rather wide shape in contrast to the very narrow shapes for the Pb-based HPs, such as $MAPbI_3$ and $CsPbI_3$.[16,51,73] This indicates that the Bi-based HP $Cs_3Bi_2I_9$ is more stable than the Pb-based HPs, for which instability is the main obstacle to their photovoltaic applications.

We then calculated the band structures of the $Cs_3Bi_2I_9$ and MoS_2 surfaces having the same planar size as the interface to determine the Fermi levels E_F, bandgaps ($E_g^{Cs_3Bi_2I_9} = 1.56$ and $E_g^{MoS_2} = 1.78$ eV) and VBM levels (E_{VBM}) (see Fig. S5, SI). To determine the E_{VBM} levels for the interface, we adopted the line-up-averaged electrostatic potential method[74,75] for the $Cs_3Bi_2I_9/MoS_2$ interface, and $Cs_3Bi_2I_9$ and MoS_2 surfaces (see Fig. S6, SI). From the obtained band structures and the work functions (calculated by $\phi = E_v - E_F$, where E_v is the vacuum level), the VBM levels were corrected to be $E_{VBM}^{Cs_3Bi_2I_9} = -4.58$ eV and $E_{VBM}^{MoS_2} = -4.79$ eV for the $Cs_3Bi_2I_9$ and MoS_2 sides, respectively.

Fig. 3(b) shows the calculated formation energies of the vacancy defects V_{Cs} and V_I as functions of E_F at the points A, B, C, D and E. The formation energies of all the vacancy defects were found to be positive, indicating that their formation is endothermic. In most cases (points A, B, C, and D), V_I^0 has the lowest formation energy, suggesting that V_I^0 is easier to form than other vacancies and thus the dominant defect at the $Cs_3Bi_2I_9/MoS_2$ interface. In particular, this argument is more evident under the I-poor/Cs-rich condition (points A, B and C). Note that in the Pb-based HPs, the V_I defect was also found to be the major defect with the lowest formation energy.[54,55] When going to the I-rich/Cs-poor condition (points D and E), it is natural to observe that the formation energy of V_{Cs} decreases while that of V_I increases, and finally V_{Cs} has a lower formation energy than V_I at point E. On the other hand, V_S was also found to have a positive formation energy, as shown in Fig. 3(c), implying that its formation at the interface is not spontaneous but endothermic in accordance with the case of the MoS_2 bulk.[76] Moreover, the formation energy of the V_S^0 state was found to be lower than those of the V_S^{1+} and V_S^{2+} states in the whole range of E_F. Interestingly, none of the thermodynamic transition levels between the differently charged defects, where the electrons could be donated or accepted, were observed, suggesting that these vacancy defects do not cause the undesirable charge recombination at the $Cs_3Bi_2I_9/MoS_2$ interface.

3.3 Interfacial charge redistribution and DOS analysis

We evaluated the charge density difference upon interface formation to gain intuitive insights into the binding strength and charge carrier transfer across the interface. Fig. 4(a) depicts the calculated planar-averaged charge density differences upon the formation of $Cs_3Bi_2I_9/MoS_2$ interfaces without and with the vacancy defects. At a glance, the charge redistribution occurs locally around the interface region, while being barely influenced by the defect formation. The charge accumulation was observed mostly in the interstitial region biased to the MoS_2 side, whereas the charge depletion was found mostly around the CsI_3 layer of the $Cs_3Bi_2I_9$ side. This observation is further clarified by the isosurface plot of the spatial electron density difference, as can be seen in Fig. 4(b), where the charge depletion (blue colour) is distributed around the I atoms of $Cs_3Bi_2I_9$, while charge accumulation (red colour) is seen around the S atoms of the MoS_2 layer (see Fig. S7 for the defective systems, SI). The observed charge redistribution indicates that the significant amount of electrons are transferred from the MoS_2 layer to the $Cs_3Bi_2I_9$ side, leading to the strong binding between them at the interface. Moreover, the interface dipole originating from this charge redistribution is expected to help the transfer of photogenerated electrons and holes as will be discussed later.

For a quantitative insight into the charge redistribution, we integrated the planar-averaged electron density difference to obtain the total transferred charge as $\Delta q = \int \Delta\bar{\rho}(z)dz$, which was further divided into the contributions from the $Cs_3Bi_2I_9$ ($\Delta q_{Cs_3Bi_2I_9}$) and MoS_2 (Δq_{MoS_2}) sides. Table 2 lists the calculated transferred charge contributions from two constituent layers in the perfect and defective interfaces. For all the cases, the $Cs_3Bi_2I_9$ part was found to have negative values whereas the MoS_2 side had positive ones. This indicates that charge is depleted at the terminal surface of $Cs_3Bi_2I_9$, while it is accumulated at the MoS_2 monolayer, resulting in the creation of an interfacial dipole moment oriented from the $Cs_3Bi_2I_9$ side to the MoS_2 side, which prevents the charge carriers from transferring across the interface. Among the different systems without and with the vacancy defects, the largest charge transfer was observed in the V_I-containing system, whereas the smallest charge transfer occurred in the V_{Cs}-containing interface.

Charge transfer often induces interface polarization, which plays an important role in the properties of a heterostructure and is quantified by the interfacial dipole moment. As mentioned above, the interfacial dipole moment, orienting

from the $Cs_3Bi_2I_9$ side to the MoS_2 side, helps the photogenerated electrons and holes move across the interface in opposite directions, thereby being favourable for preventing the recombination of photogenerated charge carriers and enhancing the photocatalytic performance in the $Cs_3Bi_2I_9/MoS_2$ heterostructure. The interface polarization induces a step in the electrostatic potential across the interface, which results in changes in the band-edge alignment. The interfacial dipole moment also originates the downward and upward band bending with the formation of a charge accumulation layer at the interface. The interfacial dipole moment, induced at the interface from the charge redistribution, was evaluated by $\Delta\mu = -\int z\Delta\bar{\rho}dz$. The calculated $\Delta\mu$ values are listed in Table 2. The V_I-containing interface was also found to have the largest $\Delta\mu$ value of 4.79 D among the interface systems under study. Meanwhile, the V_{Cs} defect causes a reduction in $\Delta\mu$ to 2.41 D. Such tendencies are consistent with the previous calculations for $CsPbI_3$/2H-MoS_2 (ref. 16) and $MAPbI_3$/2H-MoS_2 interfaces,[77] where V_I defect systems have obviously larger $\Delta\mu$ values and V_{Cs} systems have smaller $\Delta\mu$ values. When compared with those of the Pb-based HP/MoS_2 heterostructures, however, $\Delta\mu$ values are relatively larger, suggesting further improvement of photocatalytic performance in the $Cs_3Bi_2I_9/MoS_2$ interface.

In order to understand the generation and transport processes of charge carriers induced by photon incidence, we calculated the electronic density of states (DOS) of the interface systems. Fig. 4(c)–(f) display the calculated atom-projected partial density of states (PDOS) of the $Cs_3Bi_2I_9$ and MoS_2 sides and the local density of states (LDOS) along the z-axis for all the interface systems. Our calculations revealed that the lower conduction bands (CBs) responsible for the transport of photo-induced electrons are contributed from Bi and I atoms on the $Cs_3Bi_2I_9$ side and both Mo and S atoms on the MoS_2 side. From the LDOS plots, the CB edge states of MoS_2 were found to be lower in energy than those of $Cs_3Bi_2I_9$, being beneficial to the transfer of electrons photo-generated in the $Cs_3Bi_2I_9$ side to the MoS_2 side. It was found that the V_{Cs} defect causes barely any change in the electronic properties of the perfect interface system, whereas the V_I and V_S defects induce shallow trap states near the CBM level. In particular, the V_S-containing interface exhibits the trap state relatively far below the CBM level. Since trap states inside the bandgap would behave as recombination centers, they can be detrimental to the photocatalytic performance. However, it can be said that the V_S defect is difficult to be formed due to its relatively high formation energy.

3.4 Photocatalytic performance

In understanding the photocatalytic performance for HER, the band edge alignment is an important criterion. For a high HER performance, it is required that the CBM level should be higher than the hydrogen reduction potential of H^+/H_2, while the VBM level should be lower than the water oxidation potential of O_2/H_2O. Selecting the vacuum level as the reference, the hydrogen reduction potential and the water oxidation potential are calculated at different pH values as follows:[56,73]

$$E^{red}_{H^+/H_2} = -4.44\ \text{eV} + \text{pH} \times 0.059\ \text{eV}, \quad (15)$$

$$E^{oxd}_{O_2/H_2O} = -5.67\ \text{eV} + \text{pH} \times 0.059\ \text{eV}. \quad (16)$$

Once the $Cs_3Bi_2I_9$ surface is combined with the MoS_2 monolayer to build the heterostructure, some electrons are transferred to ensure the same Fermi level at the interface.[64] By using the calculated work function ϕ, we determined the Fermi levels of the $Cs_3Bi_2I_9/MoS_2$ interfaces, and then obtained the E_{VBM} and E_{CBM} values for the $Cs_3Bi_2I_9$ and MoS_2 parts, which are referenced to the vacuum level E_v (see Fig. S8 for the band structures, SI).

For the perfect interface system, the VBM and CBM levels were calculated to be −4.66 and −3.10 eV for the $Cs_3Bi_2I_9$ side and −5.18 and −3.40 eV for the MoS_2 side, respectively. Therefore, the interface was characterized as a type-II heterojunction, being significantly beneficial to the separation of electrons and holes in opposite directions, *i.e.*, preventing the recombination of charge carriers. The interfacial dipole moment induced from the charge redistribution originates the downward and upward band bending with the formation of a charge accumulation layer at the interface.[75] Fig. 5(a) shows a scheme that illustrates the generation and transfer processes of charge carriers at the heterojunction. When photons are absorbed in the $Cs_3Bi_2I_9/MoS_2$ heterojunction, electrons are excited from the VBM to the CBM on each side of the interface, due to their proper bandgaps for light absorption. Then, the electrons placed on the CBM of $Cs_3Bi_2I_9$ are attracted toward the MoS_2 side by the interface dipole, while the holes left in the VBM of MoS_2 are drawn to the $Cs_3Bi_2I_9$ side.

Fig. 5(b) illustrates the calculated band-edge alignments of the interface systems under study (see Table S4 for the corresponding numerical values, SI). In all cases, the CBM is higher than the H^+/H_2 reduction potential, indicating that the $Cs_3Bi_2I_9/MoS_2$ heterostructure has the potential to reduce H^+ to H_2. In the case of the V_I-containing interface, however, it was revealed that the band-edge alignment is not appropriate for water splitting, since the VBM is even higher than the H^+/H_2 potential. For the perfect interface and V_S-defective systems, the CBMs are lower than the O_2/H_2O potential only at pH values higher than 8, *i.e.*, in the basic environment. Therefore, they cannot produce O_2 by oxidizing H_2O under acidic conditions. With the proper band-edge alignment, the V_{Cs}-containing interface is likely to be the most promising photocatalyst for water redox reactions, especially in an acidic environment.

For further insights into the photocatalytic performance of the interface, we evaluated the Gibbs free energy for hydrogen adsorption (ΔG_{H^*}).[56] From the viewpoint of HER activity, the absolute value of ΔG_{H^*} should be as small as possible. We calculated ΔG_{H^*} for the $Cs_3BI_2I_9/MoS_2$ heterojunctions, together with the isolated $Cs_3BI_2I_9$ surface and the MoS_2 monolayer. Considering the previous result,[16] we proposed that the H atom could be adsorbed on the S atom in the top layer of the MoS_2 monolayer (see Fig. S9, SI). For the case of the $Cs_3Bi_2I_9$ surface, the adsorption site of the H atom was identified using energetic calculations. As shown in Fig. 6, the $Cs_3Bi_2I_9$ surface was found

to show the highest ΔG_{H^*} value of 2.20 eV, while the perfect heterostructure and MoS_2 monolayer have nearly the same value of 2.01 eV, which is consistent with the ΔG_{H^*} value obtained for the graphene/MoS_2 heterostructure.[78] This indicates that the formation of the interface between $Cs_3Bi_2I_9$ and MoS_2 without any defects hardly affects on the Gibbs free energy for hydrogen adsorption on the MoS_2 layer. The vacancy defect formation at the interface was found to have a positive effect on HER activity due to the lower ΔG_{H^*}, except for the V_I defect which was found to slightly increase the ΔG_{H^*} value. For V_S- and V_{Cs}-containing systems, ΔG_{H^*} was reduced to 1.48 and 0.50 eV, respectively, implying some improvement of HER performance.

For the final step, we calculated the photoabsorption spectra of the $Cs_3Bi_2I_9/MoS_2$ heterostructures without and with the interfacial vacancy defect, bulk $Cs_3Bi_2I_9$ and the MoS_2 monolayer, as shown in Fig. 7. From these spectra, we could estimate the photoabsorption edge and intensity, which are crucial factors to achieve high photocatalytic activity (see Fig. S10 for dielectric functions and other optical properties, SI). For bulk $Cs_3Bi_2I_9$ and the MoS_2 monolayer, the absorption edges were found to be 1.54 and 1.84 eV, respectively. Meanwhile, those of the heterostructures were found to be significantly shifted to the lower-energy region varying from 1.18 to 1.48 eV. Moreover, the $Cs_3Bi_2I_9/MoS_2$ heterostructures exhibited higher absorption intensities than their constituents in the visible-light and near-ultraviolet regions, representing their superior photoabsorption capability. The perfect interface has greater absorption intensity than the defective interfaces in the visible-light region, while in the ultraviolet region the defective heterostructures have higher absorption coefficients than the perfect interface. It is worth noting that among the different vacancy defects, the V_{Cs} defect induces the greatest intensity in the visible-light region. This is mainly due to the reduced bandgaps and the built-in electric field originating from the charge redistribution at the interface.[79,80]

4 Conclusions

We have systematically investigated the structural, electronic and optical properties of $Cs_3Bi_2I_9/MoS_2$ heterostructures using first-principles calculations to give a comprehensive theoretical understanding on the enhancement of photocatalytic water splitting activity for hydrogen evolution. Using the (1×1) unit cell of the $Cs_3Bi_2I_9$ (001) surface and a (7×7) cell of the 2H-MoS_2 monolayer, we built a slab model of the $Cs_3Bi_2I_9/MoS_2$ interface with a very small lattice mismatch of 0.1% without and with a vacancy defect, such as V_{Cs}, V_I and V_S. The formation and binding energies of the interface systems were calculated, confirming that these heterostructures are energetically stable. We computed the defect formation energies in the defective $Cs_3Bi_2I_9/MoS_2$ interfaces under the different growth conditions through chemical potentials of the species, finding that the V_I defect could be generated with the lowest formation energy under the I-poor/Cs-rich condition, while the V_{Cs} defect would be dominant under the Cs-poor/I-rich condition. Through the analysis of charge redistribution upon interface formation, we demonstrated that some electrons are transferred from the MoS_2 side to the $Cs_3Bi_2I_9$ side, inducing the interfacial dipole moment beneficial to preventing the recombination of photogenerated charge carriers. Our calculations of DOS and photoabsorption spectra revealed that the perfect interface system and the V_{Cs}-containing interface could be favourable for photocatalytic activity compared with other defective systems, since they do not induce shallow trap states inside the bandgap range and exhibit higher absorption intensities than others. Finally, we found that the V_{Cs}-containing heterostructure is particularly promising for improving the photocatalytic activity for hydrogen generation due to the significant reduction of the Gibbs free energy for hydrogen adsorption to 0.5 eV and the most suitable band alignment for photo-induced overall water splitting, whose band edge positions straddle the water redox potentials.

Author contributions

Yun-Sim Kim and Chol-Jun Yu developed the original project. Kyong-Mi Kim and Yun-Sim Kim performed the calculations and drafted the first manuscript. Dok-Ho Hyon and Chol-Hyok Ri contributed to useful discussions. Chol-Jun Yu supervised the work. All authors reviewed the manuscript.

Conflicts of interest

There are no conflicts to declare.

Data availability

The data are available in the supplementary information (SI) and further from the authors upon reasonable request. Supplementary information: Tables for defect position search, formation energies of the compounds, chemical potential values and band alignment, and figures for the band structure of the MoS_2 monolayer, two different sliding configurations, vacancy sites at the interfaces, the Cs-Bi-I ternary system, band structures and electrostatic potential of the interface systems, spatial charge density difference of the heterostructures with vacancy defects, adsorption geometries for hydrogen adsorption on different systems, real and imaginary parts of the dielectric function and other optical properties. See DOI: https://doi.org/10.1039/d5ra05294g.

Acknowledgements

This work is supported as part of the fundamental research project “Design of New Energy Materials” (no. 2021-12) funded by the State Commission of Science and Technology, DPR Korea. Computations in this work have been done on the HP Blade System C7000 (HP BL460c) that is owned and managed by Faculty of Materials Science, Kim Il Sung University.

References

1 N. S. Lewis, *Science*, 2016, **351**, 353.

2 P. V. Kamat and K. Sivula, *ACS Energy Lett.*, 2022, **7**, 3149–3150.
3 M. Sohail, S. Rauf, M. Irfan, A. Hayat, M. M. Alghamdi, A. A. El-Zahhar, D. Ghernaout, Y. Al-Hadeethihij and W. Lv, *Nanoscale Adv.*, 2024, **6**, 1286–1330.
4 Y. Wang, H. Suzuki, J. Xie, O. Tomita, D. J. Martin, M. Higashi, D. Kong, R. Abe and J. Tang, *Chem. Rev.*, 2018, **118**, 5201–5241.
5 Q. Hao, Y. Zhu, Y. Li, Z. Li, H. Yuan and S. Ouyang, *Ind. Chem. Mater.*, 2025, **3**, 203.
6 D. Bhanderi, P. Lakhani and C. K. Modi, *RSC Sustain.*, 2024, **2**, 265–287.
7 V. Jeyalakshmi, S. Wu, S. Qin, X. Zhou, B. B. Sarma, D. E. Doronkin, J. Kolařík, M. Šoóš and P. Schmuki, *Chem. Sci.*, 2025, **16**, 4788.
8 A. M. Huerta-Flores, F. Ruiz-Zepeda, C. Eyovge, J. P. Winczewski, M. Vandichel, M. Gaberščček, N. D. Boscher, H. J. Gardeniers, L. M. Torres-Martínez and A. Susarrey-Arce, *ACS Appl. Mater. Interfaces*, 2022, **14**, 31767–31781.
9 S. D. Tilley, *ACS Energy Lett.*, 2023, **8**, 2338–2344.
10 W. Hou, S. A. J. Hillman, S. Gonzalez-Carrero, S. Yao, H. Zhuc and J. R. Durrant, *Sustain. Energy Fuels*, 2025, **9**, 576.
11 R. Peng, X. Ma, Z. D. Hood, A. Boulesbaa, A. A. Puretzky, J. Tong and Z. Wu, *J. Mater. Chem. A*, 2023, **11**, 16714–16723.
12 S. M. Younan, Z. Li, X. Yan, D. He, W. Hu, N. Demetrashvili, G. Trulson, A. Washington, X. Xiao, X. Pan, J. Huang and J. Gu, *ACS Nano*, 2023, **17**, 1414–1426.
13 Q. Cai, I. M. McWhinnie, N. W. Dow, A. Y. Chan and D. W. C. MacMillan, *J. Am. Chem. Soc.*, 2024, **146**, 12300–12309.
14 I. M. A. Mekhemer, M. M. Elsenety, A. M. Elewa, K. D. G. Huynh, M. M. Samy, M. G. Mohamed, D. M. Dorrah, D. C. K. Hoang, A. F. Musa, S.-W. Kuo and H.-H. Chou, *J. Mater. Chem. A*, 2024, **12**, 10790–10798.
15 C. Yuan, H. Yin, H. Lv, Y. Zhang, J. Li, D. Xiao, X. Yang, Y. Zhang and P. Zhang, *J. Am. Chem. Soc. Au*, 2023, **3**, 3127–3140.
16 C.-H. Ri, H.-U. Han, Y.-S. Kim, U.-G. Jong, Y.-H. Kye and C.-J. Yu, *J. Phys. Chem. Lett.*, 2022, **13**, 4007–4014.
17 F. Xu and B. Weng, *J. Mater. Chem. A*, 2023, **11**, 4473–4486.
18 P. Wu, J. Lu, F. Xi, X. Li, W. Ma, F. Kang, S. Li, Z. Tong and Q. Zhang, *Chem. Sci.*, 2025, **16**, 4127.
19 A. Kojima, K. Teshima, Y. Shirai and T. Miyasaka, *J. Am. Chem. Soc.*, 2009, **131**, 6050–6051.
20 C. Liu, Y. Yang, H. Chen, J. Xu, A. Liu, A. S. R. Bati, H. Zhu, L. Grater, S. S. Hadke, C. Huang, V. K. Sangwan, T. Cai, D. Shin, L. X. Chen, M. C. Hersam, C. A. Mirkin, B. Chen, M. G. Kanatzidis and E. H. Sargent, *Science*, 2023, **382**, 810–815.
21 M. Saliba, *Science*, 2018, **359**, 388–389.
22 Z. Wei, Q. Zhou, X. Niu, S. Liu, Z. Dong, H. Liang, J. Chen, Z. Shi, X. Wang, Z. Jia, X. Guo, R. Guo, X. Meng, Y.-D. Wang, N. Li, Z. Xu, Z. Li, A. G. Aberle, X. Yin and Y. Hou, *Energy Environ. Sci.*, 2025, **18**, 1847–1855.
23 A. Mohandes and M. Moradi, *Mater. Adv.*, 2025, **6**, 1520–1539.
24 Y. Yang, M. Yang, D. T. Moore, Y. Yan, E. M. Miller, K. Zhu and M. C. Beard, *Nat. Energy*, 2017, **2**, 16207.
25 T. M. Brenner, D. A. Egger, L. Kronik, G. Hodes and D. Cahen, *Nat. Rev. Mater*, 2016, **1**, 15007.
26 Y. Yang, D. P. Ostrowski, R. M. France, K. Zhu, J. van de Lagemaat, J. M. Luther and M. C. Beard, *Nat. Photonics*, 2016, **10**, 53–59.
27 L. M. Herz, *Annu. Rev. Phys. Chem.*, 2016, **67**, 65–89.
28 Q. Dong, Y. Fang, Y. Shao, P. Mulligan, J. Qiu, L. Cao and J. Huang, *Science*, 2015, **347**, 967–970.
29 C. Wehrenfennig, G. E. Eperon, M. B. Johnston, H. J. Snaith and L. M. Herz, *Adv. Mater.*, 2014, **26**, 1584–1589.
30 H. Huang, B. Pradhan, J. Hofkens, M. B. J. Roeffaers and J. A. Steele, *ACS Energy Lett.*, 2020, **5**, 1107–1123.
31 X. Zhao, S. Chen, H. Yin, S. Jiang, K. Zhao, J. Kang, P. F. Liu, L. Jiang, Z. Zhu, D. Cui, P. Liu, X. Han, H. G. Yang and H. Zhao, *Matter*, 2020, **3**, 935–949.
32 T. Pal, S. Bhowmik, A. S. Tanwar, A. Suhail, N. R. Peela, C. V. Sastri and P. K. Iyer, *Energy Adv.*, 2024, **3**, 2965.
33 H. Singh, N. Minhas, G. Mustafa, G. Singh, A. Kaura and J. K. Goswamy, *RSC Adv.*, 2025, **15**, 4779.
34 Z. Guan, Y. Wu, P. Wang, Q. Zhang, Z. Wang, Z. Zheng, Y. Liu, Y. Dai, M.-H. Whangbo and B. Huang, *Appl. Catal., B*, 2019, **245**, 522–527.
35 C.-H. Kuan, Y.-A. Ko and E. W.-G. Diau, *ACS Energy Lett.*, 2023, **8**, 2423–2425.
36 U.-G. Jong, C.-J. Yu, Y.-H. Kye, S.-N. Hong and H.-G. Kim, *Phys. Rev. Mater.*, 2020, **4**, 075403.
37 A. Das, S. D. Peu, M. A. M. Akanda, M. M. Salah, M. S. Hossain and B. K. Das, *Energies*, 2023, **16**, 2328.
38 M. Miodyńska, T. Klimczuk, W. Lisowski and A. Zaleska-Medynska, *Catal. Commun.*, 2023, **177**, 106656.
39 C. Tedesco and L. Malavasi, *Molecules*, 2023, **28**, 339.
40 M. Medina-Llamas, A. Speltini, A. Profumo, F. Panzarea, A. Milell, F. Fracassi, A. Listorti and L. Malavasi, *Nanomaterials*, 2023, **13**, 263.
41 A. Pancielejko, M. Miodyńska, H. Głowienke, A. Gołabiewska, E. Gontarek-Castro, T. Klimczuk, M. Krawczyk, G. Trykowski and A. Zaleska-Medynska, *Catal. Today*, 2024, **432**, 114626.
42 T. Tang, X. Dou, H. Zhang, H. Wang, M. Li, G. Hu, J. Wen and L. Jiang, *Molecules*, 2024, **29**, 5096.
43 Y. Fan, J. Hu, T. Li, S. Xu, S. Chen and H. Yin, *Chem. Commun.*, 2024, **60**, 1004.
44 P. Giannozzi, S. Baroni, N. Bonini, M. Calandra, R. Car, C. Cavazzoni, D. Ceresoli, L. C. Guido, M. Cococcioni, I. Dabo, *et al.*, *J. Phys.: Condens. Matter*, 2009, **21**, 395502.
45 K. F. Garrity, J. W. Bennet, K. M. Rabe and D. Vanderbilt, *Comput. Mater. Sci.*, 2014, **81**, 446–452.
46 J. P. Perdew, K. Burke and M. Ernzerhof, *Phys. Rev. Lett.*, 1996, **77**, 3865.
47 J. Klimeš, D. R. Bowler and A. Michaelides, *Phys. Rev. B: Condens. Matter Mater. Phys.*, 2011, **83**, 195131.
48 J. M. Soler, E. Artacho, J. D. Gale, A. García, J. Junquera, P. Ordejón and D. Sánchez-Portal, *J. Phys.: Condens. Matter*, 2002, **14**, 2745.

49 V. Roiati, E. Mosconi, A. Listorti, S. Colella, G. Gigli and F. de Angelis, *Nano Lett.*, 2014, **14**, 2168–2174.
50 E. Mosconi, E. Ronca and F. D. Angelis, *J. Phys. Chem. Lett.*, 2014, **5**, 2619–2625.
51 Y.-S. Kim, C.-H. Ri, U.-H. Ko, Y.-H. Kye, U.-G. Jong and C.-J. Yu, *ACS Appl. Mater. Interfaces*, 2021, **13**, 14679–14687.
52 C. Freysoldt, B. Grabowski, T. Hickel, J. Neugebauer, G. Kresse, A. Janotti and C. G. Van de Walle, *Rev. Mod. Phys.*, 2014, **86**, 253–305.
53 Y.-H. Kye, C.-J. Yu, U.-G. Jong, Y. Chen and A. Walsh, *J. Phys. Chem. Lett.*, 2018, **9**, 2196–2201.
54 W.-J. Yin, T. Shi and Y. Yan, *Appl. Phys. Lett.*, 2014, **104**, 063903.
55 Y. Li, C. Zhang, X. Zhang, D. Huang, Q. Shen, Y. Cheng and W. Huang, *Appl. Phys. Lett.*, 2017, **111**, 162106.
56 F. Opoku, O. Akoto, E. E. Kwaansa-Ansah, N. K. Asare-Donkor and A. A. Adimado, *Mater. Adv.*, 2023, **4**, 1949.
57 M. Gajdoš, K. Hummer, G. Kresse, J. Furthmüller and F. Bechstedt, *Phys. Rev. B: Condens. Matter Mater. Phys.*, 2006, **73**, 045112.
58 C.-J. Yu, U.-H. Ko, S.-G. Hwang, Y.-S. Kim, U.-G. Jong, Y.-H. Kye and C.-H. Ri, *Phys. Rev. Mater.*, 2020, **4**, 045402.
59 Y. Ying, X. Luo and H. Huang, *J. Phys. Chem. C*, 2018, **122**, 17718–17725.
60 S. Saidi, S. Zriouel, L. B. Drissi and M. Maaroufi, *Phys. E*, 2018, **103**, 171–179.
61 Z. Li, B. Jia, S. Fang, Q. Li, F. Tian, H. Li, R. Liu, Y. Liu, L. Zhang, S. F. Liu and B. Liu, *Adv. Sci.*, 2023, **10**, 2205837.
62 F. Bai, Y. Hu, Y. Hu, T. Qiu, X. Miao and S. Zhang, *Sol. Energy Mater. Sol. Cells*, 2018, **184**, 15–21.
63 D. S. Koda, F. Bechstedt, M. Marques and L. K. Teles, *J. Phys. Chem. C*, 2016, **120**, 10895–10908.
64 J. Zhou, D. Li, W. Zhao, B. Jing, Z. Ao and T. An, *ACS Appl. Mater. Interfaces*, 2021, **13**, 23843–23852.
65 F. Opoku, A. Aniagyei, O. Akoto, E. E. Kwaansa-Ansah, N. K. Asare-Donkor and A. A. Adimado, *Mater. Adv.*, 2022, **3**, 4629.
66 Y. Shi, O. V. Prezhdo, J. Zhao and W. A. Saidi, *ACS Energy Lett.*, 2020, **5**, 1346–1354.
67 C.-H. Ri, S.-H. Pak, S.-I. O., C.-S. Jang, Y.-S. Kim, J.-S. Kim and C.-J. Yu, *Phys. Chem. Chem. Phys.*, 2025, **27**, 5555.
68 C. Ataca, H. Shahin, E. Aktruk and S. Ciraci, *J. Phys. Chem. C*, 2011, **115**, 3934–3941.
69 Z. Li, D. Zhoub and J. Xiangke, *Sens. Actuators, A*, 2021, **322**, 112637.
70 A. Lehner, D. Fabini, H. Evans, C. Hébert, S. Smock, J. Hu, H. Wang, J. Zwanziger, M. Chabinyc and R. Seshadri, *Chem. Mater.*, 2015, **27**, 7137–7148.
71 W. Geng, L. Zhang, Y.-N. Zhang, W.-M. Lau and L.-M. Liu, *J. Phys. Chem. C*, 2014, **118**, 19565–19571.
72 U.-G. Jong, C.-J. Yu, Y.-S. Kim, Y.-H. Kye and C.-H. Kim, *Phys. Rev. B*, 2018, **98**, 125116.
73 C.-H. Ri, S.-H. Pak, S.-I. O, C.-S. Jang, Y.-S. Kim, J.-S. Kim and C.-J. Yu, *Phys. Chem. Chem. Phys.*, 2025, **27**, 5555–5565.
74 E. Cerrato, C. Gionco, M. C. Paganini, E. Giamello, E. Albanese and G. Pacchioni, *ACS Appl. Energy Mater.*, 2018, **1**, 4247–4260.
75 C.-J. Yu, Y.-H. Kye, U.-G. Jong, K.-C. Ri, S.-H. Choe, J.-S. Kim, S.-G. Ko, G.-I. Ryu and B. Kim, *ACS Appl. Mater. Interfaces*, 2020, **12**, 1858–1866.
76 D. Cao, H. B. Shu, T. Q. Wu, Z. T. Jiang, Z. W. Jiao, M. Q. Cai and W. Y. Hu, *Appl. Surf. Sci.*, 2016, **361**, 199–205.
77 Y. Shi, O. V. Prezhdo, J. Zhao and W. A. Saidi, *ACS Energy Lett.*, 2020, **5**, 1346–1354.
78 R. K. Biroju, D. Das, R. Sharma, S. Pal, L. P. L. Mawlong, K. Bhorkar, P. K. Giri, A. K. Singh and T. N. Narayanan, *ACS Energy Lett.*, 2017, **2**, 1355–1361.
79 F. Ning, D. Wang, Y.-X. Feng, L.-M. Tang, Y. Zhang and K.-Q. Chen, *J. Mater. Chem. C*, 2017, **5**, 9429–9438.
80 C.-S. Liao, Q.-Q. Zhao, Y.-Q. Zhao, Z.-L. Yu, H. Zhou, P.-B. He, J.-L. Yang and M.-Q. Cai, *J. Phys. Chem. Solids*, 2019, **135**, 109060.